Compact Airborne C-Band Radar Sounder

Mats Jørgen Øyan, Svein-Erik Hamran, Leif Damsgård, and Tor Berger

Abstract—We describe a lightweight wideband C-band radar sounder, which is designed for use in a small unmanned aerial vehicle, primarily for measuring snow and ice. The waveform used is a gated frequency modulated continuous wave, which enables transmission at low power with relatively high energy in the compressed pulse. Gating allows use of a single antenna, reducing the influence of the direct wave on the systems' dynamic range. The radar operates at 5.3-GHz center frequency and has a bandwidth of 1 GHz, for a nominal range resolution of 15 cm in air or 12 cm in snow. Laboratory testing and airborne acquisition of data over the glacier Hardangerjøkulen show that the radar appears to work well for the intended purpose of measuring snow layer thickness.

Index Terms—CW radar, FM radar, geophysical measurements, ground penetrating radar, radar.

I. INTRODUCTION

SYNTHETIC aperture radar (SAR) images from satellites provide vast amount of data from areas covered in ice and snow, but the interpretation of these data requires *in situ* measurements. Better measurements and models of backscattering from snow, firn, and ice will greatly improve interpretation of the satellite radar data. Comparing data from the Envisat SAR with the ground-based ground penetrating radar (GPR) on Svalbard yielded promising results in determining depth penetration and backscattering properties for satellite SAR [1]–[3], but these field measurements were made from snowmobile and therefore have limited coverage. Radar sounders operated from air give information about the scattering properties of subsurface ice and snow, such as the tracked vehicle radar, but can acquire data much faster and with much more complete spatial coverage, independent of terrain.

Unmanned aerial vehicles (UAVs) have become popular both for military and civilian use. These range from full-scale airplanes such as the U.S. Air Force's Global Hawk to small micro UAVs. UAVs can be equipped with a range of sensors such as fish-eye cameras [4], cameras in the infrared spectrum for forest fire detection [5], lasers for mapping archaeological sites [6], and meteorological sensors [7] and radars [8]. A small UAV has the advantage of being lighter than an ordinary plane, easier to deploy, and can fly lower and in more hostile environments than a manned aircraft [9]. The drawbacks are less space and electrical power available than in a manned aircraft.

The radar described in this paper is designed to fill the gap between satellite remote sensing data, ground-vehicle-based GPR, and ice cores from drilling. While providing better resolution and flexibility than satellites, the UAV has much better coverage than ground-based radar data.

II. RADAR DESIGN

The radar is designed to be flown in a small UAV, which means some compromises must be made. It must be lightweight and energy efficient and has to fit physically into a small UAV. It also has to be able to work autonomously while flying. To reduce cost for each radar system, one of the design considerations was to use low-cost off-the-shelf components.

C-band is chosen because it is the same frequency band as the Envisat SAR, allowing the data from these two sensors to be compared with regard to penetration and backscattering.

The radar is based on a previous design. The low-frequency part is identical to the ultrawideband radar described in [10] and is already well tested. The software and the RF part of the radar are similar but were redesigned for C-band. A top-level schematic of the radar system is shown in Fig. 1. The radar parameters are presented in Table I.

A. Waveform

The waveform used is a gated frequency modulated continuous wave (FMCW), which allows efficient sampling of all the transmitted energy [11]. The transmitted signal is a sinusoid whose frequency linearly increases with time (see Fig. 2). A direct digital synthesizer (DDS1) generates a signal in the frequency range of 9.6–11.6 MHz, as a linear sweep between the two frequencies. The signal from the DDS is connected to a phase-locked loop (PLL), which controls a voltage-controlled oscillator (VCO), effectively multiplying the reference signal from the DDS to generate a signal between 4.8 and 5.8 GHz. This signal is then split in two, one part going toward the antenna and the other back to the phase comparator. At any given time, only one frequency is transmitted. When the maximum frequency is reached, the radar returns to the start frequency, and the process starts again. The time used to return to the start frequency is t_r in Fig. 2. One whole measurement takes t_{Mf}.

The radar output power can be adjusted in software between -11 and $+20$ dBm. The signal is gated by the antenna switch.

The signal reflected from the ground is amplified and gated in the same way as the transmitted signal. The receiver gain can be adjusted in 1-dB steps between 30 and 61 dB before it is

This article has been accepted for inclusion in a future issue of this journal. Content is final as presented, with the exception of pagination.

2   IEEE TRANSACTIONS ON GEOSCIENCE AND REMOTE SENSING
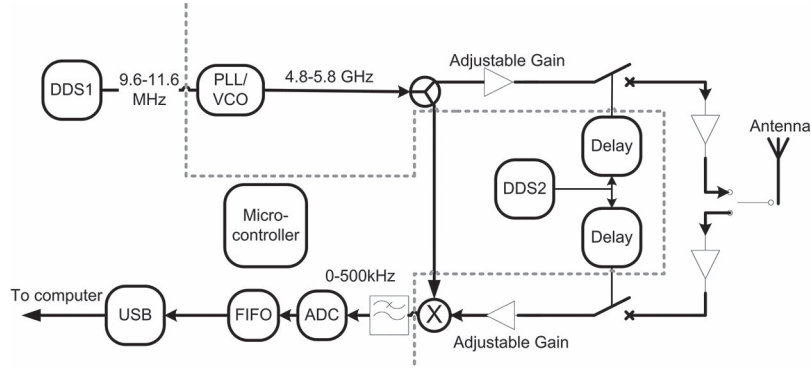
Fig. 1.   Radar schematic. The dotted line shows the separation of the low-frequency data collection board and the RF board. The single pole, double throw switch, amplifiers, and antenna are external components.

TABLE I
RADAR PARAMETERS

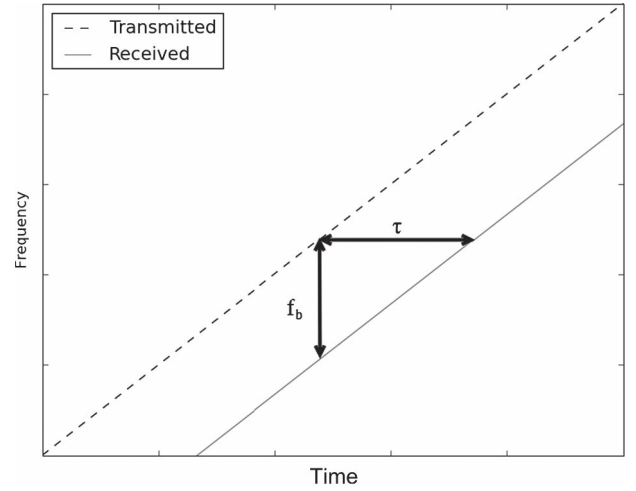| Waveform	Gated FMCW
Center frequency	5,3 GHz
Transmitted power	≈ 20 dBm
Bandwidth	1 GHz
Sweep time	5 ms
Gate frequency	1 MHz
PRF	20 Hz
AD	16 bit
Sampling clock	1 MHz
Size	21x20x8 cm
Weight	< 3 kg

Fig. 3.   Part of the transmitted and received signals from the target.
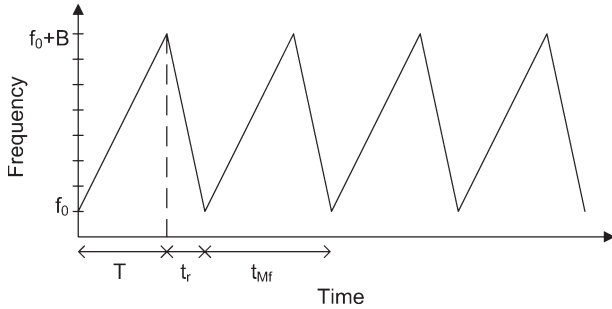

Fig. 2.   Transmitted frequency versus time. During T, the frequency is linearly increased while data are being collected. During t_r, the radar is reset. The duration of a complete measurement cycle is $T + t_r = t_{Mf}$.

mixed with the transmitted signal, resulting in a beat frequency. The beat frequency is

$$f_b = \frac{B \cdot \tau}{T} \qquad (1)$$

where B is the radar bandwidth, τ is the two-way travel time (TWTT) to the target, and T is the sweep time. The TWTT is

$$\tau = \frac{2 \cdot r}{v} \qquad (2)$$

where r is the range to the target, and v is the wave propagation speed in the medium. This is illustrated in Fig. 3. Here, we zoom in on the transmitted and received signals from a target with a TWTT of τ. The received signal is shifted in frequency
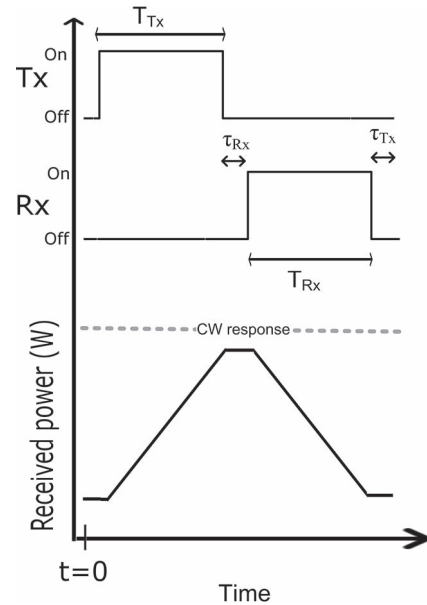

Fig. 4. Tx and Rx gating signals with the tunable parameters and the effect of gating window on received power as a function of time [12]. The tunable delay symbols are defined in the text.

compared with the transmitted signal, and the difference between these two frequencies is the beat frequency. Longer delay τ give a higher beat frequency f_b.

This article has been accepted for inclusion in a future issue of this journal. Content is final as presented, with the exception of pagination.

ØYAN *et al.*: COMPACT AIRBORNE C-BAND RADAR SOUNDER 3

Fig. 5. Radar setup as seen through the passenger door of the aircraft. The gray aluminium box contains the radar, which is controlled from a laptop by the operator sitting at the rear of the plane. The hole on the floor is covered by a Plexiglass window, which has little attenuation for the the radiated wave.

The beat frequency is low-pass filtered and sampled at a rate of 1 MHz, which is much lower than required to sample the received signal directly without downmixing. The maximum beat frequency is

$$f_{b\text{Max}} = \frac{f_s}{2} \tag{3}$$

where f_s is the sampling frequency. The maximum instrumented range is

$$r_{\text{Max}} = \frac{f_{b\text{Max}} \cdot T \cdot v}{2 \cdot B}. \tag{4}$$

For the sounder, $f_s = 1$ MHz, $T = 5$ ms, $v = 0.3$ m/ns in free space, and $B = 1$ GHz. This means that the maximum range in free space is 375 m.

B. Gating

FMCW radars transmit and receive at the same time, whereas for chirp radars, the whole waveform is transmitted before the receiver is turned on. This means that FMCW radars in general can be used at closer range than chirp radar systems. However, in FMCW radars, the direct signal from the transmitter to the receiver antennas limits the system dynamic range. A gated FMCW radar uses a gating signal to turn on and off the transmitter and the receiver chain. The radar range response is multiplied by a convolution between the transmitter and re-

ceiver gating signals. The resulting response is shown in Fig. 4. Close targets, such as the direct wave, are attenuated, whereas the weaker subsurface returns are less attenuated, compared with nongated FMCW radar.

The gating signal is generated by a separate DDS (DDS2 in Fig. 1). This allows for quick changes in the gating frequency, which ranges between 1 and 20 MHz, and is controlled by software.

The gating signal is shown in Fig. 4. The variables that can be changed are T_{Tx} and T_{Rx}. They are given by the gating frequency and the delays τ_{Tx} and τ_{Rx}, which can be controlled separately. In this system, the delays are set to $\tau_{Tx} = 0$ ns and $\tau_{Rx} = 0$ ns, and the gating frequency is set to 1 MHz. Maximum received power is at half the gating period, whereas the direct signal between antennas is effectively removed. Because the radar never sends and receives at the same time, only one antenna is used, saving both space and weight (see Fig. 5 for the radar setup).

C. Bandwidth and Center Frequency

The nominal resolution of the radar is

$$\Delta r = \frac{v}{2B} \tag{5}$$

which is the -4-dB width of the impulse response. In free space, the velocity v is c, i.e., the speed of light. In other

This article has been accepted for inclusion in a future issue of this journal. Content is final as presented, with the exception of pagination.

4   IEEE TRANSACTIONS ON GEOSCIENCE AND REMOTE SENSING

materials, the velocity is given as

$$v = \frac{c}{\sqrt{\varepsilon_r}} \qquad (6)$$

where ε_r is the relative permittivity. Snow has a ε_r of about 1.5, depending on snow density. This gives our system a resolution of approximately 12 cm in snow.

D. Sampling and Processing

The sampling frequency is 1 MHz. Since sweep time is 5 ms, each trace gives 5000 samples. The pulse repetition frequency (PRF) of the system is 20 Hz, allowing the platform to move 1.5 m between each trace when moving at 30 m/s.

The resolution of the analog-to-digital (A/D) converter is 16 bits, with a theoretical dynamic range of 96.4 dB. After A/D conversion, the data are forwarded to a first-in–first-out buffer. A single board computer reads the data through a USB interface and stores it on a solid-state disk. Because the disk is based on Flash memory, it is less sensitive to temperature variations and vibration than a traditional hard drive. The computer is fanless, making the whole system free from moving parts.

The data collected are in the frequency domain and are transformed to the time domain through a Fourier transform. The data are multiplied by a Blackman window function and zero padded before the Fourier transform to get a better visual representation. The absolute value from the Fourier transform is used, giving the envelope of the returned signal. A program was written to translate the collected data, which is in a proprietary form to a format readable by Reflexw [13], a commercial GPR processing program with a large toolkit for postprocessing.

III. EXPERIMENTAL RESULTS

The radar system has been tested in the laboratory and in a Cessna 172 small aircraft. It has been prepared for use in a UAV, but it is less complicated to do testing from a manned aircraft than a UAV. When operated from a manned aircraft, data can be analyzed in real time, and the radar settings can be altered during flight to do experiments and optimizations.

A. Laboratory Experiments

One way to test a radar is to use a delay line, simulating a reflector at a distance equal to the cable length. This way, only the radar itself is measured. To avoid saturation of the receiver, attenuation was added to the delay line.

The delay line with attenuators was connected to the antenna switch (see Fig. 6). The attenuation of the cable and attenuators was measured with a network analyzer to be 50 dB, and the total delay for the cable with attenuators was measured to be 205.5 ns. Without termination at the other end of the cable, the radar signal reflected off the end and returned to the receiver. The reflected signal has been attenuated a total of -100 dB when entering the receiver. The average transmitted power of the radar was -5 dBm over the whole frequency sweep. With this information, we calibrated the radar receiver, knowing that the received power was $-5-100 = -105$ dBm.
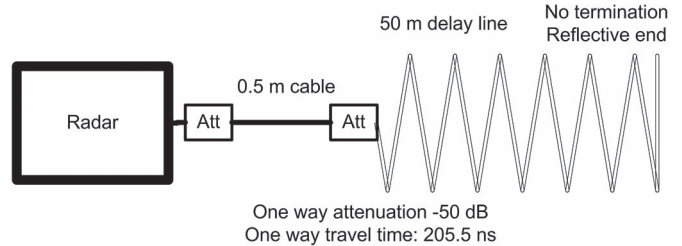

Fig. 6.   Configuration of the laboratory test. The signal is transmitted through a 50.5-m-long cable with a 205.5-ns delay. Because the end is not terminated, the signal is reflected and returns to the receiver. The total attenuation is measured to be 100 dB.
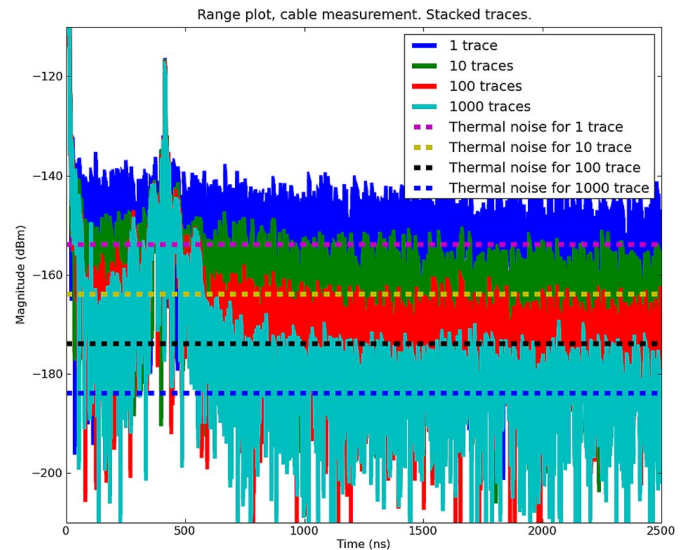

Fig. 7.   Beat frequency translated into the time domain, for the whole instrumented range. Multiple traces are stacked to show that the radar measurements are coherent. The cable reflection is located at 415 ns, corresponding to the TWTT of the 205.5-ns attenuating cable. The remaining 4 ns represent delays in radar system. The spurious signals seen for longer integration times are from the sweep oscillator used in the prototype.

Results from the laboratory test (see Fig. 7) show how the delay cable is equivalent to a target at $t = 415$ ns. The difference to the delay determined from a network analyzer is 4 ns and is attributed to the internal delay from cabling within the radar. The reflector is 13.5 dB lower than the calculated power because of the gating attenuation and window function in the processing. Range resolution is defined as the width of the impulse at -4 dB below the peak. Fig. 8 shows a zoomed view of the cable return with a horizontal line showing the -4-dB level. A window function is used to reduce sidelobes; the Blackman window function used here leads to approximately two times worse resolution than if we had only used a square window. The total width of the reflection above the -4-dB level is 1.91 ns, which translates to 28.6 cm in free space or 23.4 cm in ice. Other window functions could be used to improve resolution if sidelobe suppression is not a concern.

The thermal noise power N in decibels per milliwatt is given by

$$N = 10 \log 10(kT_n B_i \cdot 1000) \qquad (7)$$

This article has been accepted for inclusion in a future issue of this journal. Content is final as presented, with the exception of pagination.

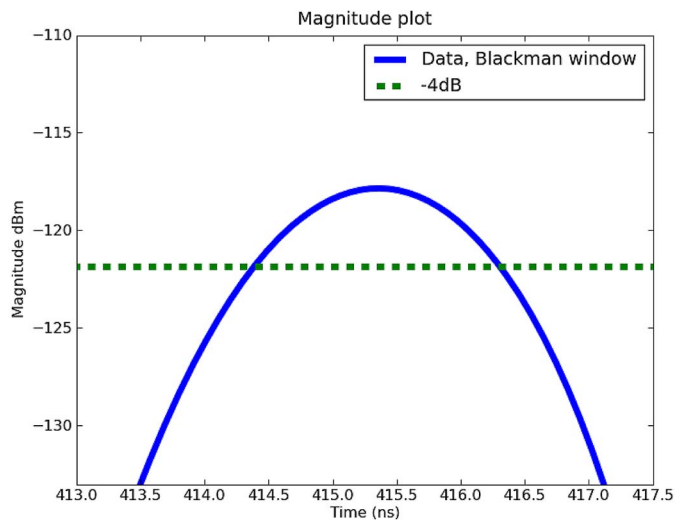ØYAN *et al.*: COMPACT AIRBORNE C-BAND RADAR SOUNDER
5

Fig. 8. Close-up view of cable reflection (see Fig. 7). The TWTT is 415.4 ns. The 4-dB width of the main lobe is 1.91 ns, giving a resolution of 28.6 cm in free space.

Fig. 9. Map showing the location of Hardangerjøkulen, radar flight lines. The orange part of the line indicates measured profile (see Fig. 10).

where k is the Boltzmann's constant, T_n is the temperature in kelvins, and B_i is the receiver bandwidth. For our FMCW radar, B_i is

$$B_i = \frac{B_{IF}}{T f_s N_s} \tag{8}$$

where B_{IF} is the bandwidth of the low-pass mixer in front of the A/D converter, and N_s is the stack factor. In our radar, $B_{IF} = 500$ kHz, $T = 5$ ms, and $f_s = 1$ MHz. $N_s = 1$ for single trace measurements. The Fourier transform used to transfer the samples into the time domain is effectively a sum over all the samples. This means that the noise bandwidth is reduced to $(500 \text{ kHz}/5000) = 100$ Hz for one trace. This gives a thermal noise level of $N \approx -154$ dBm, which can be further improved by stacking traces. Fig. 7 shows that for each multiplication of 10 of N_s, the noise goes down 10 dB, as expected from noncorrelated thermal noise. The calculated thermal noise is plotted and is 2 dB below the average measured noise.

The radar was submitted to a test in a climate chamber. A long delay line was connected and left at room temperature. The radar was cooled to -45 °C and operated for 1 h without problems.

B. Field Test

We performed a flight test with the C-band radar sounder in a Cessna 172 small aircraft. The airplane was modified to accommodate the radar sounder. The front passenger seat was removed, and a rectangular-shaped hole was made on the floor of the aircraft. A mounting frame with a Plexiglas window was made to allow the radar antenna to radiate out of the hole while avoiding too much wind in the cabin. The radar setup is shown in Fig. 5. Power for the radar was provided by separate batteries, i.e., not connected to the airplane power supply. The radar was equipped with a horn antenna (type 201187) from Tecom [14] and flown over Hardangerjøkulen, a plateau glacier in
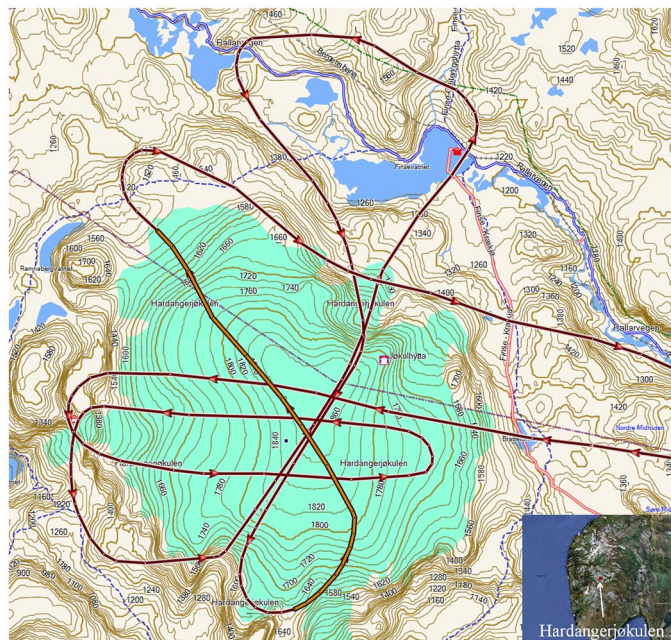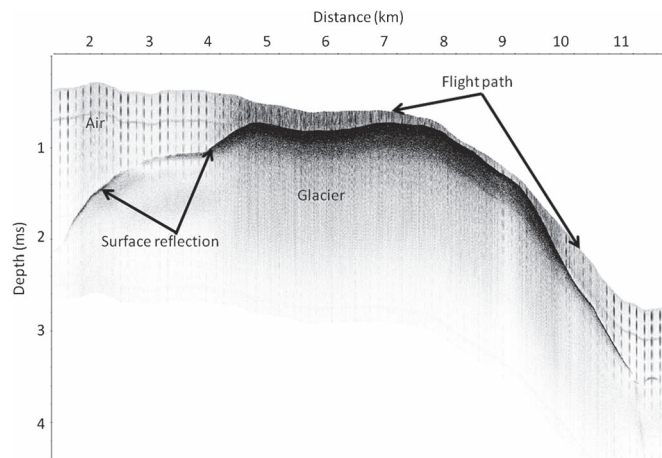

Fig. 10. Radar profile from Hardangerjøkulen. This plot shows the whole radar profile corrected for topography.

the western part of Norway. The glacier covers approximately 73 km^3, and its highest point is 1863 m above sea level. Several profiles were collected in a pattern shown in Fig. 9. A sample radar profile is indicated on the map and plotted in Fig. 10.

The profile has been corrected for the flight path using Global Positioning System altitude measurements, giving the correct topography of the glacier surface. The periodical noise in the data between the airplane and the surface is believed to be the noise from the airplane and was not seen in the data when the airplane engine was turned off on the ground. The surface reflection is strong and shows that the radar is working properly. The plots in Figs. 11 and 12 show zoomed parts of the profile. In these plots, we see more detail in the data, and several internal layers can be identified. Ground proof was not collected, but the Norwegian Water Resources and Energy Directorate (NVE)

This article has been accepted for inclusion in a future issue of this journal. Content is final as presented, with the exception of pagination.

6   IEEE TRANSACTIONS ON GEOSCIENCE AND REMOTE SENSING
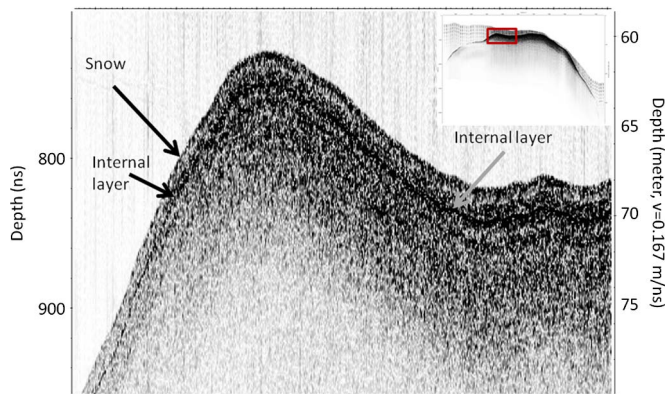

Fig. 11.   Zoomed-in part of the radar profile. Internal layers of snow, firn, and ice in the glacier can be seen.
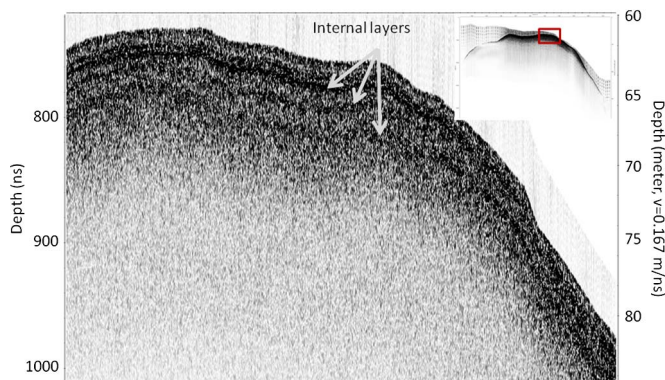

Fig. 12.   Zoomed-in part of the radar profile. Internal layers of snow, firn, and ice in the glacier can be seen.

reported snow depths of 1–2 m in the lower parts of the glacier and 2–3 m in the upper parts [15], at the end of the same winter in which we did our measurements. Their measured snow density was 530 kg/m^3, which means the end of the winter snow layer would vary from 14 ns in the lower parts to 56 ns higher up on the glacier [16]. In our data, we see a strong reflection at 10 ns at the start of the profile and 20 ns on the top of the glacier, somewhat less than expected from the NVE measurements. However, our data were collected earlier in the winter than the NVE data, which may account for this difference.

IV. CONCLUSION

In this paper, we have shown the design and implementation of a compact C-band radar sounder for UAV applications. The gated FMCW waveform allows it to operate close to the target, which means that the transmitted power can be low. The gating makes it possible to use single antenna operation. The radar is small and lightweight and can be flown in a UAV. We have shown that it works well from a small aircraft and can be used to image subsurface layers in snow and ice. In a UAV application, the radar will be flown closer to the ground, resulting in a smaller radar footprint. The UAV can also fly slower, which can improve signal-to-noise ratio. The radar has good coherency, and the resolution is as expected from the bandwidth.

This C-band sounder will enable a UAV to do snow and ice measurements over difficult-to-reach areas, such as avalanche-prone or crevassed areas, and will allow acquisition of data over large areas more easily and quickly than making comparable measurements on the ground.

REFERENCES

[1] K. Langley, S.-E. Hamran, K. Hogda, R. Storvold, O. Brandt, J. Kohler, and J. Hagen, "From glacier facies to SAR backscatter zones via GPR," *IEEE Trans. Geosci. Remote Sens.*, vol. 46, no. 9, pp. 2506–2516, Sep. 2008.

[2] K. Langley, S.-E. Hamran, K. Hogda, R. Storvold, O. Brandt, J. Hagen, and J. Kohler, "Use of C-band ground penetrating radar to determine backscatter sources within glaciers," *IEEE Trans. Geosci. Remote Sens.*, vol. 45, no. 5, pp. 1236–1246, May 2007.

[3] K. Langley, P. Lacroix, S.-E. Hamran, and O. Brandt, "Sources of backscatter at 5.3 GHz from a superimposed ice and firn area revealed by multi-frequency GPR and cores," *J. Glaciol.*, vol. 55, no. 190, pp. 373–383, Apr. 2009.

[4] A. Gurtner, D. Greer, R. Glassock, L. Mejias, R. Walker, and W. Boles, "Investigation of fish-eye lenses for small-UAV aerial photography," *IEEE Trans. Geosci. Remote Sens.*, vol. 47, no. 3, pp. 709–721, Mar. 2009.

[5] L. Merino, F. Caballero, J. Martinez-de Dios, and A. Ollero, "Cooperative fire detection using unmanned aerial vehicles," in *Proc. IEEE ICRA*, Apr. 2005, pp. 1884–1889.

[6] K. Lambers, H. Eisenbeiss, M. Sauerbier, D. Kupferschmidt, T. Gaisecker, S. Sotoodeh, and T. Hanusch, "Combining photogrammetry and laser scanning for the recording and modelling of the late intermediate period site of Pinchango Alto, Palpa, Peru," *J. Archaeol. Sci.*, vol. 34, no. 10, pp. 1702–1712, Oct. 2007.

[7] A. van den Kroonenberg, T. Martin, M. Buschmann, J. Bange, and P. Vörsmann, "Measuring the wind vector using the autonomous mini aerial vehicle M2AV," *J. Atmos. Ocean. Technol.*, vol. 25, no. 11, pp. 1969–1982, Nov. 2008.

[8] W.-Q. Wang, Q. Peng, and J. Cai, "Waveform-diversity-based millimeter-wave UAV SAR remote sensing," *IEEE Trans. Geosci. Remote Sens.*, vol. 47, no. 3, pp. 691–700, Mar. 2009.

[9] C. Eheim, C. Dixon, B. M. Argrow, and S. Palo, "Tornadochaser—A remotely-piloted UAV for in situ meteorological measurements," presented at the 1st Unmanned Aerospace Vehicles, Systems, Technologies, and Operations Conference and Workshop, Portsmouth, VA, USA, May, 2002.

[10] M. Oyan, S. Hamran, L. Hanssen, T. Berger, and D. Plettemeier, "Ultra-wideband gated step frequency ground-penetrating radar," *IEEE Trans. Geosci. Remote Sens.*, vol. 50, no. 1, pp. 212–220, Jan. 2012.

[11] M. J. Øyan, S.-E. Hamran, T. Berger, and L. Hanssen, "Characterisation of ultra wideband frequency modulated and step frequency radar with range gating," in *Proc. IASTED ARP*, Jul. 2009, pp. 129–134.

[12] S. E. Hamran, D. T. Gjessing, J. Hjelmstad, and E. Aarholt, "Ground penetrating synthetic pulse radar: Dynamic range and modes of operation," *J. Appl. Geophys.*, vol. 33, no. 1–3, pp. 7–14, Jan. 1995.

[13] J. Sandmeier, ReflexW Version 5.0. Windows 9x/NT/2000/XP-program for the processing of seismic, acoustic or electromagnetic reflection, refraction and transmission data, 2008.

[14] *Dual Polarized Quad-Ridged Horns*, i. Tecom Industries, Thousand Oaks, CA, USA, Aug. 2013.

[15] B. Kjøllmoen, L. M. Andreassen, H. Elvehøy, M. Jackson, and R. Giesen, "Glaciological investigations in Norway in 2010," Norwegian Water Res. Energy Directorate, Oslo, Norway, 2011.

[16] M. E. Tiuri, A. Sihvola, E. Nyfors, and M. Hallikaiken, "The complex dielectric constant of snow at microwave frequencies," *IEEE J. Ocean. Eng.*, vol. 9, no. 5, pp. 377–382, Dec. 1984.

Mats Jørgen Øyan was born in Oslo, Norway, in 1981. He received the M.Sc. degree in computer science from the Norwegian University of Science and Technology (NTNU), Trondheim, Norway, in 2006. He is currently working toward the Ph.D. degree in sounding radar systems at the Norwegian Defence Research Establishment (FFI), Kjeller, Norway.

Svein-Erik Hamran received the M.Sc. degree in technical physics from the Norwegian University of Science and Technology (NTNU), Trondheim, Norway, in 1984 and the Ph.D. degree in applied physics from the University of Tromso, Tromsø, Norway, in 1990.

From 1985 to 1996, he was with the Environmental Surveillance Technology Programme. From 1989 to 1990, he was a Visiting Scientist with Service d'Aeronomie, Centre National de la Recherche Scientifique, Paris, France. Since 1996, he has been a Chief Scientist with the Norwegian Defence Research Establishment, Kjeller, Norway, managing radar programs. From 2001 to 2011, he was an Adjunct Professor with Near Surface Geophysics, Department of Geosciences, University of Oslo, Oslo, Norway, where he has also been an Adjunct Professor with the Department of Informatics since 2011. He is a Coinvestigator on the European Space Agency (ESA) satellite ROSETTA experiment Comet Nucleus Sounding Experiment by Radiowave Transmission and a Coprincipal Investigator on the Water Ice and Subsurface Deposit Observation on Mars experiment on the ESA ExoMars satellite. His main research interests are ultrawideband radar design and radar imaging and modeling in medical and ground penetrating radar.

Tor Berger was born in Tromsø, Norway, in 1968. He received the M.Sc. and Ph.D. degrees in applications of the wavelet transform in image processing from the University of Tromsø, Tromsø, in 1992 and 1996, resepectively.

Since 1996, he has been with the Norwegian Defence Research Establishment, Kjeller, Norway, working in different fields such as weapon effects, security sensors, and signal processing. After a period of working with research planning and strategy, he is currently involved in radar signal processing related to ultrawideband systems and inverse synthetic aperture radar.

Leif Damsgård received the M.Sc. and Ph.D. degrees in microelectronics from the University of Oslo, Oslo, Norway, in 1985 and 1991, respectively.

His research interests have been in analog, radio frequency, and microwave circuit design and in microwave electronics systems.